Combining near-infrared tomography and magnetic resonance imaging to study *in vivo* breast tissue: implementation of a Laplacian-type regularization to incorporate magnetic resonance structure

Ben Brooksby
Shudong Jiang
Hamid Dehghani
Brian W. Pogue
Keith D. Paulsen
Dartmouth College
Thayer School of Engineering
8000 Cummings Hall
Hanover, New Hampshire 03755

John Weaver
Christine Kogel
Steven P. Poplack
Dartmouth Hitchcock Medical Center
Department of Diagnostic Radiology
Lebanon, New Hampshire 03756

Abstract. An imaging system that simultaneously performs near infrared (NIR) tomography and magnetic resonance imaging (MRI) is used to study breast tissue phantoms and a healthy woman *in vivo*. An NIR image reconstruction that exploits the combined data set is presented that implements the MR structure as a soft-constraint in the NIR property estimation. The algorithm incorporates the MR spatially segmented regions into a regularization matrix that links locations with similar MR properties, and applies a Laplacian-type filter to minimize variation within each region. When prior knowledge of the structure of phantoms is used to guide NIR property estimation, root mean square (rms) image error decreases from 26 to 58%. For a representative *in vivo* case, images of hemoglobin concentration, oxygen saturation, water fraction, scattering power, and scattering amplitude are derived and the properties of adipose and fibroglandular breast tissue types, identified from MRI, are quantified. Fibroglandular tissue is observed to have more than four times as much water content as adipose tissue, almost twice as much blood volume, and slightly reduced oxygen saturation. This approach is expected to improve recovery of abnormalities within the breast, as the inclusion of structural information increases the accuracy of recovery of embedded heterogeneities, at least in phantom studies.
[DOI: 10.1117/1.2098627]

Keywords: cancer; breast; magnetic resonance; *a priori*; diffuse; adipose; glandular; near infrared.

Paper SS04250R received Dec. 16, 2004; revised manuscript received Mar. 4, 2005; accepted for publication Mar. 23, 2005; published online Oct. 10, 2005.

1 Introduction

Recently, near infrared (NIR) imaging and spectroscopy have demonstrated an ability to quantify intrinsic tissue chromophore concentrations and scattering properties, thereby providing valuable functional information.[1–8] Imaging systems that measure light transmission in the NIR wavelength range and utilize model-based computational methods can generate spatially resolved absolute images of oxyhemoglobin, deoxyhemoglobin, and water as well as scattering parameters affected by cellular and subcellular structural elements. This technology is well suited to the study of breast tissue, and spatial and temporal contrasts in these properties may be uniquely useful for diagnosing disease. The application of NIR tomography will likely be important, yet customized imaging systems which couple to ultrasound, magnetic resonance imaging (MRI), or x-ray methods must be developed to evaluate and exploit this potential. The clinical standards for breast cancer detection—ultrasound, contrast-enhanced MRI, and x-ray mammography—provide high spatial resolution but comparatively little information about molecular-level changes in breast tissue.[9,10] X-ray mammography, the most common form of breast cancer screening, has high sensitivity in women with fatty breast composition,[11] but low sensitivity in radiographically dense breasts, and low positive predictive value. It also uses ionizing radiation, and requires uncomfortable breast compression. Biopsy is generally required to determine malignancy in most women with an abnormal mammogram. Adjunctive noninvasive imaging modalities are often required to characterize suspicious abnormalities, especially in women with radiographically dense tissue. There is considerable potential for functional NIR imaging to distinguish breast cancer noninvasively, yet this modality has consistently suffered from low spatial resolution.[12–14] This paper reports on the combination of NIR tomography with MRI for the investigation of breast tissue properties to provide fundamentally new information by exploiting the strengths of each modality. Such hybrid approaches could generate image data that achieves the intrinsically high optical contrast known to

Address all correspondence to Brian Pogue, Thayer School of Engineering, Dartmouth College, 8000 Cummings Hall, Hanover, NH 03755. Tel.: (603) 646-3861; Fax: (603) 646-3856; E-mail: pogue@dartmouth.edu

1083-3668/2005/10(5)/051504/10/$22.00 © 2005 SPIE

exist in tumors on the spatial scale of structural MRI. The potential benefits of this type of hybrid method can only be evaluated once prototype systems are developed and optimized in a clinical setting.

In both research and clinical applications, multimodality imaging is increasingly being used to interrogate tissue morphology and function simultaneously because of the inherently optimized coregistration. Structure and function of tissue afford different physical bases for contrast and combinations have proven beneficial in the diagnosis and management of disease.[15] With the advent of molecular medicine, a transition in diagnostic interpretation becomes possible based on biochemical perturbations that occur in disease, frequently in the absence of changes in anatomic structure. A prominent example is hybrid position emission tomography/computed tomography (PET/CT) systems, where coupling structure to functional images has been more informative when interpreting the metabolic data.[16] Hybrid imaging systems also avoid complications associated with tissue movement between separate exams, which reduce coregistration accuracy and thus degrade the diagnostic value of the image fusion.[17]

This paper explores the combination of structural and functional imaging into a single platform for the study of breast tissue. Functionally, NIR contrast mechanisms in tissue are dominated by elastic Mie-like scattering.[18] Measured signals are highly sensitive to tissue concentrations of oxyhemoglobin, deoxyhemoglobin, and water. Structurally, contrast in MRI derives from intrinsic tissue factors related to micromagnetic structural inhomogeneities. Relaxation times vary substantially for different tissues and are strongly dependent on their physical characteristics.

In addition to coregistration, data sets from combined NIR and MRI imaging offer other synergistic benefits, namely anatomical priors (from high-spatial-resolution MRI) enhance NIR (i.e., high-contrast-resolution) image reconstruction. NIR spectroscopy is biochemically rich, but spectroscopic imaging is hindered by the highly scattered photon paths that reduce resolution in tissue. The most widely adopted approach to this problem incorporates parameter estimation strategies based on models of light propagation in tissue. The estimation task is sensitive to small perturbations in the light measurements, not all of which are caused by the intrinsic changes in tissue optical properties. Experience has shown that significant improvement in the stability and accuracy of the reconstruction process can be obtained by including prior anatomical/optical information.[19–25]

Techniques for incorporating this information are relatively new, and are the subject of active research in a variety of disciplines, including medical imaging,[26–28] industrial process imaging,[29] and geophysical surveying,[30] yet there is no clear consensus on the optimal approach. Spatial resolution and quantitative image accuracy can be improved when the appropriate constraints, derived from *a priori* information, are applied. However, these priors and constraints can take a wide variety of forms, and currently there are few broadly adopted conventions even though it is commonly accepted that such constraints offer significant potential value. It is less well appreciated that misguided constraints can lead to gross solution errors that are detrimental to the image outcome. To date, NIR techniques have been combined with several high-spatial-resolution, structure-bearing imaging modalities including x-ray tomosynthesis,[21] ultrasound,[31] and MRI (Refs. 27, 32, and 33) to study human tissues and small animals. Past experiences have contributed to a variety of imaging systems, imaging geometries, and numerical reconstruction techniques, but have not led to a consensus on the optimal way of applying *a priori* derived constraints.

This paper describes the clinical application of our breast imaging system—a highly sensitive multispectral frequency domain NIR tomography system that is compatible with the magnetic field environment inside a standard full-body MRI scanner. The combined data set offers measurements of light transmission through the full volume of the breast in a planar anatomically coronal geometry and a high-resolution MRI of that same volume. Algorithmic procedures for exploiting both NIR and MRI data to reconstruct first optical property (absorption and reduced scattering coefficient) distributions, and then tissue chromophores and scatter parameters are described and validated with phantom studies. The impact of including the MRI component of this imaging platform is shown for a human volunteer. The segmentation of adipose from fibroglandular tissue is examined and analyzed. The combined imaging system could become a valuable tool for characterizing the optical signatures of normal breast tissue, benign breast conditions, and breast cancer. Currently, NIR exams occur predominantly in laboratories that are developing the technology under National Institutes of Health (NIH) research funding. Considering that many women commonly undergo MRI breast exams, and that the system described here can be seamlessly integrated into these procedures, it provides an excellent opportunity to determine the optimal way to integrate prior spatial information into NIR tomography. This type of combined system may prove to be an important bridge that carries NIR imaging methods from the lab into accepted clinical application.

2 Methods

2.1 *Hardware*

The imaging system used records measurements of NIR light transmission through a pendant breast in a planar, tomographic geometry. The patient lies inside a 1.5-T whole-body MRI (GE Medical Systems) and the two data types (i.e., NIR and MRI) are acquired simultaneously. The system is shown in Fig. 1, and was described in detail by Brooksby et al.[34] Figure 1(a) shows the portable cart, which contains the light generation and detection hardware subsystems. Six laser diodes (660 to 850 nm) are amplitude modulated at 100 MHz. The bank of laser tubes is mounted on a linear translation stage, which sequentially couples the activated source into 16 bifurcated optical fiber bundles. The central seven fibers deliver the source light while the remaining fibers collect transmitted light and are coupled to photomultiplier tube (PMT) detectors located in the base of the cart. The fibers are positioned in a plane spanning the circumference of a pendant breast, and for each activated source, measurements of the amplitude and phase shift of the 100-MHz signal are acquired from 15 locations around the breast. Figure 1(b) shows a photograph of the MR-compatible fiber positioning system anchored inside an open architecture breast array coil (MRI De-

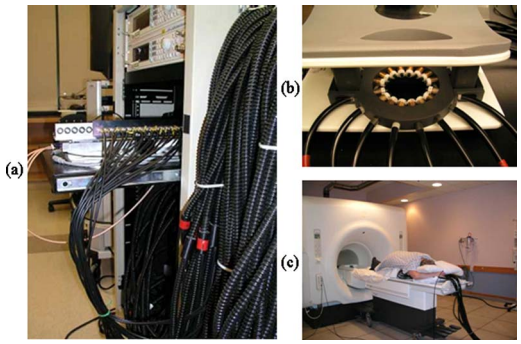

Fig. 1 (a) Photograph of the portable cart housing the NIR light generation and detection hardware. The cart remains outside of the rf-shielded MR chamber, and optical fibers extend 13 m to the MRI patient bed. On the retracted shelf, a linear translation stage sequentially couples one activated laser diode to each of the 16 optical fibers that contact the breast. (b) MR-compatible fiber-patient interface, made of polyvinyl chloride (PVC), is mounted inside a high-resolution MR breast coil. Compression springs ensure light contact between each fiber and the patient's skin. (c) A patient volunteer lying prone on the combined MRI-NIR bed prior to her exam.

vices). The vertical position of the imaging plane is manually adjusted, and contact with the breast is maintained automatically using bronze compression springs.

2.2 *Image Formation*

It is well established that in the interaction of NIR light with tissue, scattering dominates over absorption. Under these conditions, light transport can be effectively modeled using the diffusion equation over moderately large distances.[35,36] Analogous to the hardware approach, a frequency-domain diffusion model is used to simulate measured signals for any specified distribution of absorption and reduced scattering coefficients, μ_a and μ_s', within an imaged volume. This is given by

$$-\nabla\cdot D(r)\,\nabla\,\Phi(r,\omega)+\left[\mu_a(r)+\frac{i\omega}{c}\right]\Phi(r,\omega)=S(r,\omega), \tag{1}$$

where $S(r,\omega)$ is an isotropic light source at position r, $\Phi(r,\omega)$ is the photon density at r, c is the speed of light in tissue, ω is the frequency of light modulation, and $D=1/[3(\mu_a+\mu_s')]$ is the diffusion coefficient. The reduced scattering coefficient is given by $\mu_s'=\mu_s(1-g)$, where g is the mean cosine of the single scatter function (the anisotropy factor), and μ_s is the scattering coefficient. A type III boundary condition is applied as

$$\Phi+\frac{D}{\alpha}\hat{n}\cdot\nabla\Phi=0, \tag{2}$$

where α is a term that incorporates reflection as a result of refractive index mismatch at the boundary, and $\hat{n}$ is the outward-pointing normal to the boundary.

Equation (1) can be viewed as a nonlinear function of the optical properties. Its solution is represented as a complex-valued vector, $\mathbf{y}^*=F(\mu_a,D)$, having real and imaginary components that are transformed to logarithm of the amplitude and phase in the measurements. The phase shift of the signal provides data that is dominated by the optical path length through tissue, while the amplitude of the transmitted light provides information about the overall attenuation of the signal. These measurements constitute the dataset necessary for successful estimation of both absorption and reduced scattering coefficients.

Data acquired by the detection system is processed with a finite element method (FEM)-based reconstruction algorithm to generate tomographic images of μ_a and μ_s'. In the image reconstruction, a Newton-minimization approach developed by Paulsen and Jiang[37] is used to seek a solution to

$$(\hat{\mu}_a,\hat{D})=\min_{\mu_a,D}\{\|\mathbf{y}^*-F(\mu_a,D)\|+\lambda\|(\hat{\mu}_a,\hat{D})-(\mu_{a0},D_0)\|\}, \tag{3}$$

where $\|\cdot\|$ represents the square root of the sum of squared elements. This is the so-called Tikhonov approach,[38] and λ is a weighting factor of the difference between the current values of the optical properties and their initial estimates. The magnitude of this objective function is sometimes referred to as the projection error and provides a value for determining the convergence of the iterative solution. Its minimum is evaluated by setting first derivatives with respect to μ_a and D equal to zero. This leads to a set of equations that is solved iteratively, using the following matrix equation,[39] derived from Eq. (3):

$$\delta\mu=(\mathbf{J}^T\mathbf{J}+\lambda\mathbf{I})^{-1}\mathbf{J}^T[\mathbf{y}^*-F(\mu_a,D)]+\lambda(\mu-\mu_0). \tag{4}$$

At each iteration, the new set of μ_a and D values is updated by $\mu_a^{i+1}=\mu_a^i+\delta\mu_a^i$, and $D^{i+1}=D^i+\delta D^i$, where i is the index for the iteration number, $\mathbf{J}$ is the Jacobian matrix for the diffusion equation solution, and $\mathbf{J}^T\mathbf{J}$ is ill-conditioned and therefore regularized through the addition of $\lambda\mathbf{I}$, where $\mathbf{I}$ is an identity matrix. Regularization is implemented in a Levenberg-Marquardt algorithm where λ starts at a high value (typically 10 times the maximum value of the diagonal of $\mathbf{J}^T\mathbf{J}$) and is systematically reduced at each iteration. In Eq. (4), μ_0 is the initial estimate of optical properties input into the iterative estimation process, and is a form of prior information.[40] Here, the initial estimate is determined through a data calibration procedure which assumes a homogeneous property distribution.[41] In our experience, the last term in Eq. (4), $\lambda(\mu-\mu_0)$, has little effect on the solution due to the small size of both λ and $(\mu-\mu_0)$, especially at late iterations, and can be ignored. If this term were included, and λ were not reduced with each iteration, the current optical property estimate would not stray very far from the homogeneous initial estimate. This is not desirable when reconstructing heterogeneities. Efforts are currently being made toward the generation heterogeneous initial guesses, which could make the inclusion of this extra term beneficial.

2.3 *Inclusion of Priors*

Image reconstruction techniques which incorporate prior knowledge of tissue structure have been largely developed for nuclear imaging over the last decade.[26,42–45] Anatomical information is generally used to adjust image smoothness and reduce noise levels during reconstruction. Most of the approaches to this problem are based on Bayesian estimation

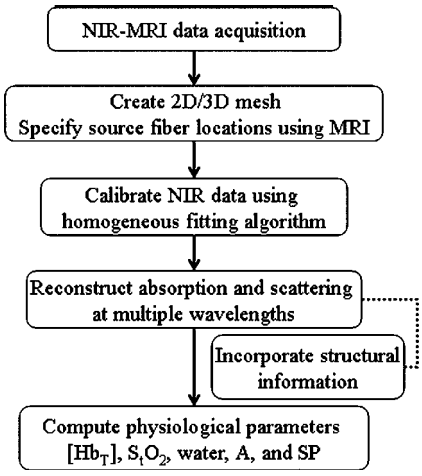

Fig. 2 Flow chart tracking the key steps associated with the use of the combined NIR-MRI imaging system.

techniques. Prior information consists of anatomical boundaries that are likely to correspond to discontinuities in an otherwise spatially smooth radionuclide distribution. In the reconstructed image, neighboring pixels within homogeneous regions should have similar intensity levels. In regions which exhibit distinctly different tissue characteristics, smoothing across their shared boundary should be limited. Improving NIR reconstructions by incorporating prior knowledge of tissue structure available from MRI data has been explored in previous work at Dartmouth[13,19,32,40,46] and by other authors.[20–22,27,31,33,47,48] Our early work involved using high-resolution MRI to construct an accurate rendering of the full volume of breast tissue probed by NIR light. Following the lead of Ntziachristos et al.[27] and Zhu et al.[31] it was further assumed that optical contrast correlated to MRI contrast, and the number of property estimates was dramatically reduced.[40] While generally effective in simulation studies, and for reconstructing simple phantom geometries containing a single discrete heterogeneity (i.e., inclusion), this method was vulnerable to overbiasing the inverse solutions toward the assumed distributions. Sensitivity to noise in the data and error in the region designation caused this "parameter reduction" algorithm to be unreliable when imaging complex and layered phantoms. Here, we describe an improved technique that guides the iterative evolution of reconstruction, but does not impose the rigid constraint of interregion homogeneity. This algorithm is still able to detect optical coefficient patterns that violate the prior information. Similar to the strategy outlined by Li et al.,[21] this is accomplished through regularization. The benefits of the implementation described here is that reconstruction is not a complex multistep process. For the first time, NIR measurements taken in a full tomographic geometry can be used to generate high-resolution functional images through a flexible procedure, regardless of arbitrary tissue structures.

A priori information can be incorporated directly through the objective function by formulating the minimization of a two term functional:[25]

$$(\hat{\mu}_a,\hat{D}) = \min_{\mu_a,D}\{\|\mathbf{y}^* - F(\mu_a,D)\| + \alpha\|\mathbf{L}[(\hat{\mu}_a,\hat{D}) - (\mu_{a0},D_0)]\|\}. \quad (5)$$

The constant α balances the effect of the prior with the model-data mismatch. The filter matrix $\mathbf{L}$ is generated using MRI-derived priors and effectively relaxes the smoothness constraints at the interface between different tissues, in directions normal to their common boundary. The effect on image quality is similar to that achieved through total variation minimization schemes.[49] This procedure, however, is more robust and can easily encode internal boundary information from MR images. Each node in the FEM mesh is labeled according to the region, or tissue type, with which it is associated (in the MR image). For the i'th node of n in region $N, L_{i,l}=1$. When nodes i and j are in the same region, $L_{i,j}=-1/n$, otherwise $L_{i,j}=0$. The solution to Eq. (5) is again accomplished with a Newton-minimization approach, that produces the update equation

$$\delta\mu = (\mathbf{J}^T\mathbf{J} + \alpha\mathbf{L}^T\mathbf{L})^{-1}[\mathbf{J}^T[\mathbf{y}^* - F(\mu_a,D)] + \Lambda], \quad (6)$$

which is iteratively solved. Note $\mathbf{L}^T\mathbf{L}$ approximates a second-order Laplacian smoothing operator within each region separately. This construction of $\mathbf{L}$ has proved flexible and effective, as demonstrated in the phantom studies shown in Sec. 3, but other forms can easily be implemented and evaluated. Similarly to Eq. (4), the last term, $\Lambda=\alpha\mathbf{L}^T\mathbf{L}[(\mu_{ai},D_i) - (\mu_{a0},D_0)]$, has been ignored in the results presented here.

Simulation studies were performed to characterize the effect of $\mathbf{L}$ and α on the quality and quantitative accuracy of reconstructed images, and to establish a value of α that can be used routinely. Data was generated from numerical phantoms with a variety of heterogeneity patterns—ranging from a simple circular anomaly in a homogeneous background (similar to the physical phantom in Fig. 4 in Sec. 3.2) to irregular distributions of regions with two or three different properties (similar to the complexity of the breast in Fig. 5 in Sec. 3.3). Noise (1 to 2%) was added to simulated data to better replicate experimental conditions. Error was also added to the *a priori* region designation, to account for the small loss of resolution when spatial information is transferred from MR images to FEM meshes. Images were reconstructed from this data using a range of α from 1 to 100. A high α value increases the impact of the spatial prior, leading to images with sharper internal boundaries, but could negatively bias solutions if this prior is not correct. By accounting for the different sources of error that are present when data is acquired with the system presented here, simulation results indicate that setting α to 10 times the maximum value of the diagonal of $\mathbf{J}^T\mathbf{J}$ optimizes image quality and accuracy regardless of the level of geometric complexity present in the area under investigation. Unlike λ in Eq. (4), α does not decrease during the iterative solution process.

2.4 *Spectral Decomposition*

The absorption coefficient at any wavelength is assumed to be a linear combination of the absorption due to all relevant chromophores in the sample:

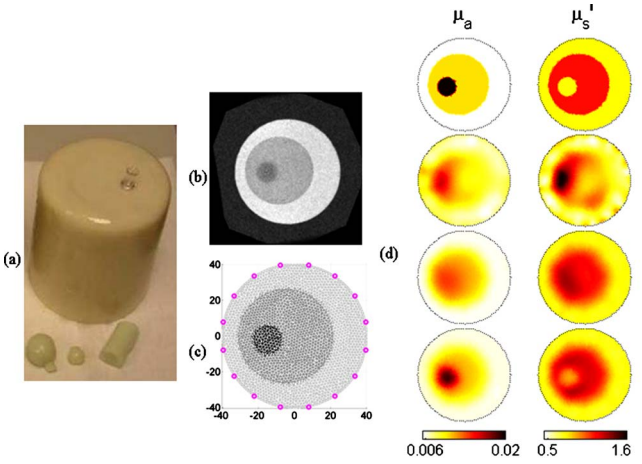

Fig. 3 (a) Photograph of a gelatin phantom and a variety of inclusions (small gelatin spheres and a cylinder with different optical properties); (b) MRI showing a cross section of the cylindrical phantom, visible in the MRI are three types of gel; and (c) finite element mesh segmented according to the MRI intensity. The optical fiber source/detectors marked around the circumference are specified with millimeter accuracy. The axes are in millimeters, showing the full diameter of the phantom to be 82 mm. (d) Reconstructed images of the absorption and reduced scattering coefficients for this phantom. The top pair of images shows the true distribution, the second pair shows the reconstructions that do not use *a priori* information, the third pair shows reconstruction in which two layers were assumed from the MRI (i.e., the inclusion was ignored), and the bottom pair shows reconstructions in which the full MRI is used. When the full compliment of prior information is used, root mean square image error decreases 43% for absorption and 55% for scattering.

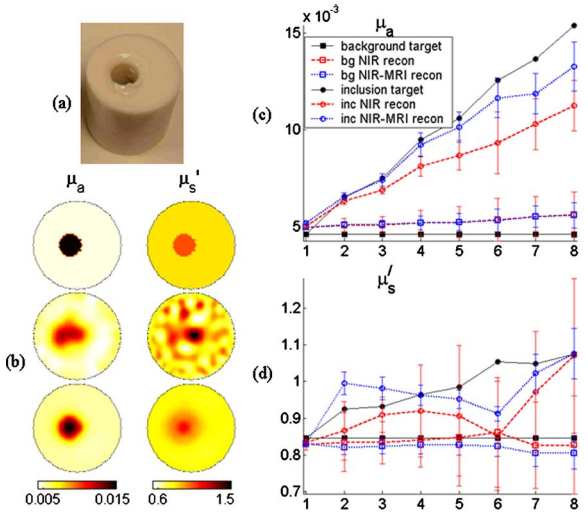

Fig. 4 (a) Photograph of the homogeneous gelatin phantom with a 22-mm cylindrical cavity slightly off-center and (b) reconstructed images of the absorption and reduced scattering coefficients for this phantom when an intralipid solution with 3:1 absorption contrast fills the opening. The top pair of images shows the true distribution, the middle pair shows the reconstructions which result when *a priori* information is not used, and the bottom pair results when prior information about the size and location of the anomaly is incorporated. When prior information is used, root mean square image error decreases 26% for absorption and 58% for scattering. Image artifacts appear in the form of artificial background heterogeneity when priors are not utilized. A more accurate estimate of the true optical properties, and shape of the inclusion, is obtained with the MR-guided iterative algorithm. (c) and (d) Absorption and reduced scattering coefficients respectively for both the background (bg) and the inclusion (inc), recovered using the two algorithms for eight intralipid solutions with different absorption coefficients. The images in (b) correspond to solution 8, on the far right of (c) and (d).

$$\mu_a(\lambda) = \sum_{i=1}^{N} \varepsilon(i,\lambda) C_i, \tag{7}$$

where λ is the molar absorption spectra, and C is the concentration of each chromophore.[18] In the presented analysis, the concentrations of three chromophores—oxyhemoglobin (HbO_2), deoxyhemoglobin (Hb), and water (H_2O)—are estimated. Hence, given μ_a at the k'th pixel for multiple wavelengths, a linear inversion of Eq. (7) determines the array of C values

$$C_k = \mathbf{E}^{-1} \mu_{a,k}, \tag{8}$$

representing the concentrations of the three chromophores. In Eq. (8), $\mathbf{E}$ is the matrix of molar extinction coefficients having elements $\varepsilon(i,\lambda)$, for the i'th chromophore at different wavelengths.

The spectral character of the reduced scattering coefficient also provides information about the composition of the tissue. From an approximation to Mie scattering theory, it is possible to derive a relation between μ_s' and wavelength given by

$$\mu_s'(\lambda) = A\lambda^{-\mathrm{SP}}, \tag{9}$$

where SP is the scattering power and A is the scattering amplitude[50] (which depend on scatterer size and number density). Typically, large scatterers have lower SP and A values. These scattering parameters appear to reflect variations in structural breast composition associated with age and radiographic density.[8,51]

2.5 *Phantom Studies*

Single- and multilayered phantoms were fabricated from gels with different optical properties using heated mixtures of water (80%), gelatin (20%) (G2625, Sigma Inc.), India ink or blood (for absorption), and titanium dioxide powder (for scatter) (TiO_2, Sigma Inc.) that are solidified by cooling to room temperature. Optically distinct layers were fabricated by successively hardening gel solutions containing different amounts of ink and TiO_2. True properties were estimated by measuring a large cylindrical sample of each material.[41] Because these phantoms are water-based, they are well suited for testing a combined NIR-MRI system. To increase MRI contrast between different gels in multilayered phantoms, 0.001 to 0.005 g/ml Omniscan™ (gadodiamide) was added.

Two studies with gelatin-based phantoms were performed. The first examined spatial resolution, while the second assessed quantitative accuracy as a function of inclusion contrast. The phantom imaging procedure is outlined in Fig. 2. Data acquisition is followed by automated MR image processing and FEM mesh generation. The MRI is segmented via automatic thresholding and edge detection, and pixels of similar intensity are assumed to represent the same material or

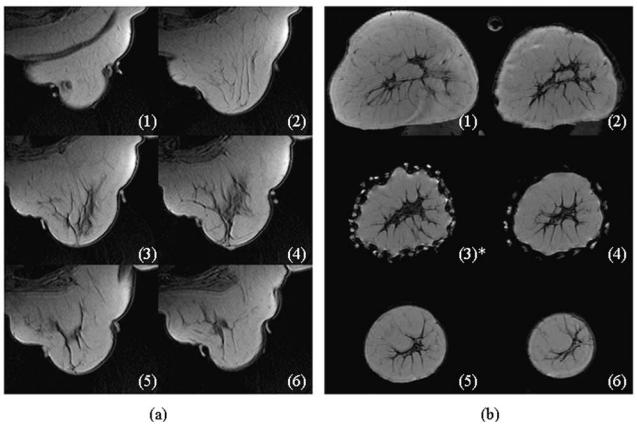

Fig. 5 MRI slices of a normal breast for a representative subject with scattered radiographic density, imaged with the NIR-MRI system. (a) Anatomically axial (cranial-caudal; slice 6 to slice 1) T_1-weighted MR images. Slice thickness is 5 mm and the space between slices is 10 mm. Toroidal fiducial markers surround the optical fibers approximately 1 cm from the tip, and appear as bright spots outside of the tissue. (b) Oblique coronal T_1-weighted MR images of the same breast. Slice (1) is toward the chest wall, and slice (6) is toward the nipple. Slice thickness is 2 mm and the space between slices is 10 mm. Coronal slice (3)* is the plane of the optical fibers. A region of glandular tissue (dark greay) appears surrounded by a layer of adipose (light gray). This slice was used to set construct the FEM mesh in order to reconstruct the optical property distributions (see Fig. 6).

tissue. This material information is transferred to the FEM mesh as a "region" label. NIR data are calibrated using a reference measurement of a homogeneous phantom to correct for variation between the 16 optical channels.[41,52] Optical property reconstruction is performed on the appropriate mesh, containing the same number of distinctly visible regions as the MRI. Appropriate labels are given to the mesh so that *a priori* guidance is automatic. If optical property images are obtained at multiple NIR wavelengths, spectral analysis is performed and chromophores/scatter parameters are calculated.

2.6 *Human Subject Studies*

All human studies are carried out under informed consent according to protocol approved by the Institutional Review Board at Dartmouth. Although we present a single case study here, several women participated in the study. Healthy volunteers were recruited from a pool of women having received a routine screening mammography at Dartmouth Hitchcock Medical Center. The subject lies prone on the scanner table with her breast pendant into the open architecture breast array coil, and a nurse or MRI technician operates the optical fiber positioning system to establish uniform tissue contact at sixteen points around the perimeter of the breast. Once inside the bore of the 1.5-T magnet, MRI and NIR data are acquired simultaneously. The MRI protocol typically involves two imaging sequences. First, scout images are acquired in three orthogonal planes to localize the orientation of the optical fiber array. Second, a T_1-weighted volume of the entire breast is obtained with each slice oriented parallel to the plane of the optical fibers. NIR data acquisition is automated via Labview software (National Instruments) executing on a separate computer. Measurements are recorded serially at six wavelengths, and a typical exam lasts approximately 15 min. In the case study presented here, five wavelengths of NIR data were collected. Once the patient exits the magnet, the procedure outlined in Fig. 2, including MRI-guided NIR image reconstruction and spectral decomposition is performed. Images of physiological parameters, total hemoglobin concentration ($[Hb_T]$), percent blood oxygen saturation (S_tO_2), water fraction (H_2O), scattering amplitude (A), and scattering power (SP) can be generated approximately 15 min after data acquisition.

3 Results

3.1 *Phantom Imaging: Spatial Resolution*

A two-layer gelatin phantom with a cylindrical inclusion embedded inside the inner layer was used to evaluate the ability of the NIR-MRI system to resolve this type of structure. A photograph of the phantom is shown in Fig. 3(a). Figure 3(b) shows an MRI slice through the phantom at the height of the inclusion, and Fig. 3(c) shows the FEM mesh, and optical fiber locations. Each gel layer possessed a different absorption (outer layer, 0.0055 mm^{-1}; inner layer, 0.01 mm^{-1}; inclusion, 0.02 mm^{-1}) and reduced scattering coefficient (outer layer, 0.75 mm^{-1}; inner layer, 1.2 mm^{-1}; inclusion, 0.75 mm^{-1}). The outer and inner layers extended the full height of the phantom (10 cm) while the inclusion (height, 2.5 cm; diameter, 1.5 cm) was embedded half-way from top to bottom.

Figure 3(d) contains reconstructed images of the optical properties at a 785-nm wavelength. The top pair of images shows the true distribution of absorption and reduced scattering coefficients. The second pair of images indicates the reconstructions that result from the solution of Eq. (3), which is the standard Newton-minimization and does not use *a priori* information. Although not presented here, a parameter reduction algorithm that reconstructs a single absorption and reduced scattering coefficient for each region was also used. The estimated properties do not match the true phantom properties. The maximum absorption was localized to the inner layer rather than the inclusion, and the maximum scatter was localized to the inclusion rather than the inner layer. The third pair of images results from the solution of Eq. (5), where the layered MRI data was used to form the regularization matrix. In this case, to illustrate the performance of the algorithm when prior information is incomplete or incorrect, the presence of the inclusion was not specified. The bottom pair of images results from the solution of Eq. (5), where the full MRI data, including the presence of the inclusion, was used to form the regularization matrix. Clearly these images more accurately represent the true property distributions. The iterative reconstruction process is terminated automatically when the projection error reaches its minimum. For both algorithms this occurred at iteration 11.

3.2 *Phantom Imaging: Contrast Resolution*

To characterize the performance of the system and the quality of the defined algorithm, a phantom with inclusions of different contrast was imaged. A gelatin solution ($\mu_a = 0.005\ mm^{-1}$, $\mu_s' = 0.85\ mm^{-1}$) was hardened inside an 82-mm cup, with a 22-cm-diam cylindrical rod included in

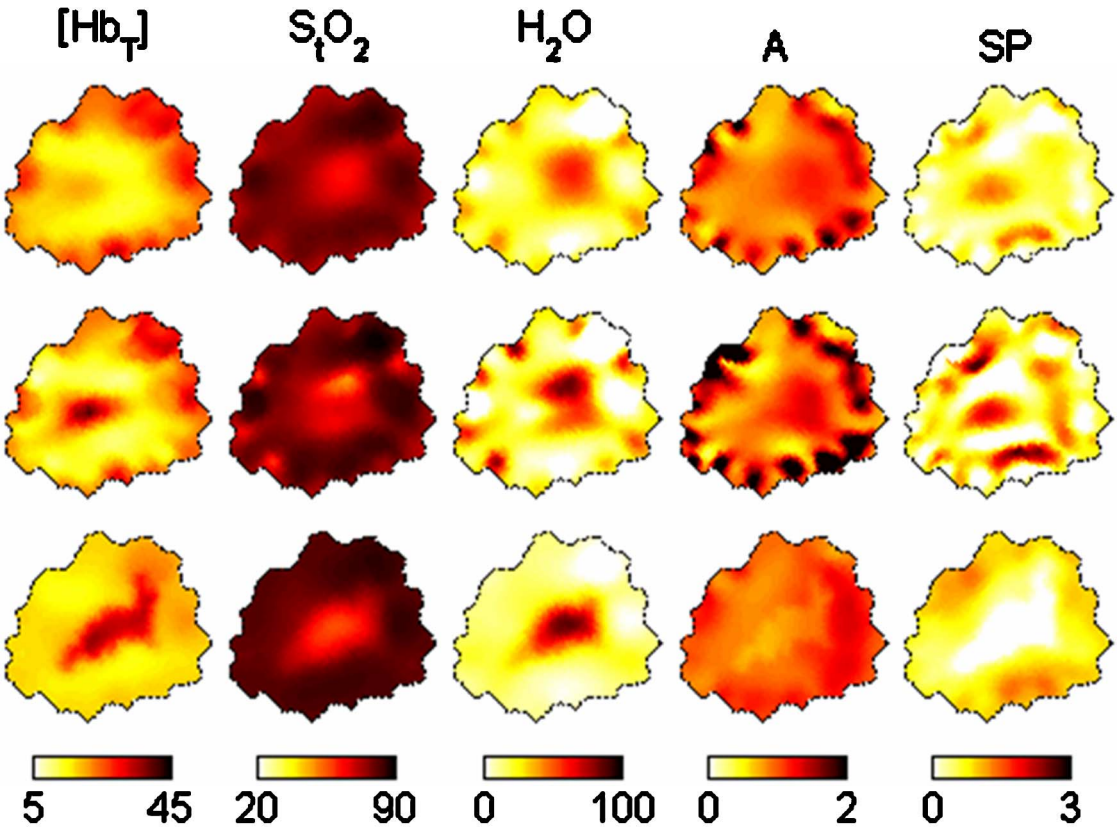

Fig. 6 NIR-MRI results for a representative subject. These tomographic NIR images correspond to MRI slice (3)* in Fig. 5(b). NIR chromophore concentrations and scattering parameters were derived from spectral analysis and Mie theory. Three sets of images are shown. Two sets were derived from absorption and reduced scattering coefficients that were reconstructed with a standard Newton-minimization algorithm, unconstrained by priors obtained from MRI. The first (top) used the fifth iteration while the second (middle) used the projection error minimum as a stopping criteria (iterations 9 to 11). The third set (bottom) incorporated regional structure visible in the MRI to guide optical property estimation and projection error minimum stopping criteria. When the algorithm is unconstrained by MR, intertissue contrast appears to develop at later iterations, but noise also increases (especially in scatter). Using MRI constraints, artifacts are suppressed and images exhibit high contrast and good resolution.

the interior. After the gelatin hardened, the rod was removed and the empty column was filled with intralipid solutions having absorption coefficients ranging from 0.005 to 0.015 mm^{-1}. A photograph of the phantom is shown in Fig. 4(a). Another photograph (not shown) taken of the phantom in the imaging array was used as a surrogate MRI. This was used to define *a priori* information of the phantom's structure, and provided the necessary detail to carry out region of interest analysis to assess reconstruction accuracy. Figure 4(b) presents target values of absorption and reduced scattering coefficients (top) for a phantom with 3:1 absorption contrast, along with the corresponding reconstructions based on Eq. (3) (middle) and Eq. (5) (bottom). Figures 4(c) and 4(d) report the absorption and reduced scattering coefficient averages for both the background and the inclusion when recovered with the two algorithms. In general, the inclusion absorption coefficient is more accurately estimated when the MRI information is utilized in the reconstruction algorithm. Additionally, the spatial variation in both properties is reduced.

3.3 *Representative Breast Results*

Here we present in detail the study of a healthy volunteer whom we examined with the combined NIR-MRI imaging system. Anatomically axial and oblique coronal T_1-weighted gradient echo MR images are shown in Figs. 5(a) and 5(b), respectively. The woman had breasts with scattered radiographic density (i.e., fatty tissue containing scattered fibroglandular densities). The MR slices reveal an area of blood vessels and vascularized glandular tissue near the center of the breast (dark in the MR image), surrounded by a subsurface layer of adipose tissue (light gray in the MR image). Fiducial markers, attached to each fiber are visible just outside the breast surface. In Fig. 5(b), image slice (3)* corresponds to the optical measurement plane. An FEM mesh for image reconstruction was generated by segmenting adipose and glandular tissue in this image slice, based on image intensity. The mesh accurately describes the convoluted outer breast boundary, the size and shape of the glandular region, and the location of the 16 NIR measurement sites. Along with the MRI, NIR transmission data (amplitude and phase) was measured at five wavelengths (661, 785, 808, 826, and 849 nm). Spectral deconvolution was performed from images of μ_a and μ_s' reconstructed at these wavelengths. The images of NIR chromophore concentrations and scattering properties are shown in Fig. 6. The three sets of images correspond to spectral analysis using different μ_a or μ_s' reconstructions. The

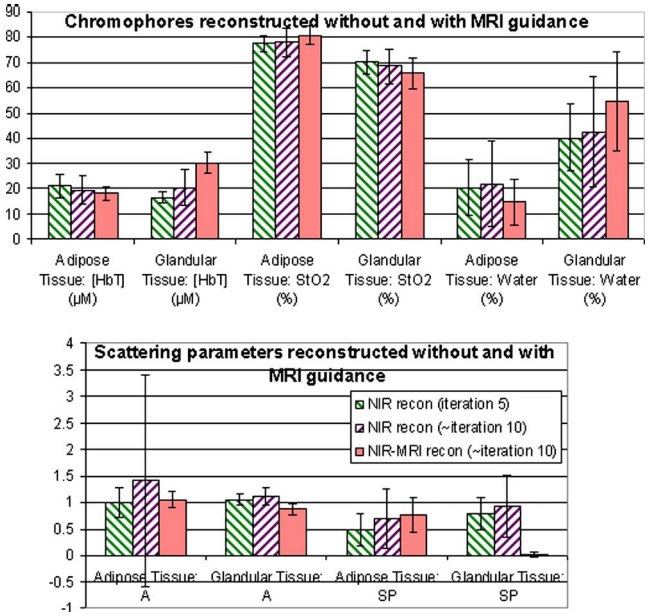

Fig. 7 Graphs of reconstructed tissue properties from Fig. 6. Total hemoglobin concentration ($[Hb_T]$), oxygen saturation (S_tO_2), water, scattering amplitude (A), and scattering power (SP) are reported separately for adipose and fibroglandular tissue, again as defined from the spatial pattern of gray-scale intensity from the simultaneously acquired MRI. Error bars represent the standard deviation of property values within a particular tissue. For each chromophore, MR-guided NIR reconstruction decreases intratissue variation and increases intertissue contrast. For scattering parameters, MR-guidance primarily reduces the size of the error bars.

images presented estimate total hemoglobin concentration $[Hb_T]$, blood oxygen saturation S_tO_2, water H_2O, scattering amplitude A, and scattering power SP. The first set of images (top row) results when the solution of Eq. (3) is stopped prior to convergence at iteration 5, which is the approach we have utilized in our previous NIR breast studies. The second set of images (in the middle row) results when the algorithm continues to the projection error minimum (iterations 9 to 11). The third set of images (bottom row) is obtained from the convergent solution of Eq. (5). In this case the full knowledge of tissue structure, provided by MRI, is brought to bear in the NIR image reconstruction. When the algorithm is unconstrained by MR, intertissue contrast appears to develop at later iterations, but noise also increases. The estimates that rely on constraints from MRI data suppress artifacts and produce images that exhibit high contrast and resolution. Average values of each of these parameters are tabulated in Fig. 7, for both the adipose and the glandular tissue regions, and for all three reconstruction approaches.

4 Discussion

NIR tomography is potentially an important adjunct to anatomical imaging because of the possibility of adding unique information to the characterization of diseased tissue. This paper explored the implementation of simultaneous NIR-MRI imaging methods that were used to study breast tissue *in vivo*. There is little debate that knowledge of tissue structure can constrain/guide NIR image reconstruction to improve spatial resolution and quantitative accuracy of recovered physiological parameters. However, there is considerably less certainty about how best to incorporate the information. In this paper, we developed a full regularization matrix where locations are linked within the same tissue type. The validation of the approach was demonstrated through phantom experiments designed to mimic the layered geometry apparent in many breasts.

The first phantom study, described in Sec. 3.1, evaluated spatial resolution of the combined NIR-MRI imaging system. The results shown in Fig. 3(d) indicate that the MR-guided iterative algorithm performed much better than the standard reconstruction approach in terms of the ability to resolve layer location and interior heterogeneities. In particular, it produced absorption and reduced scattering coefficient images which accurately represented the layered optical contrast (μ_a, 4:2:1; μ_s', 1:1.6:1). When the MRI data was neglected, and amplitude and phase data were reconstructed with a standard Newton type reconstruction, the calculated images only slightly resembled the true spatial structure. Additionally, quantitative accuracy suffered. The scattering of the inclusion appeared to increase relative to the inner layer while in actuality it decreased. The root mean square (rms) error of the recovered distributions of the absorption and reduced scattering coefficients were estimated to be 0.0023 and 0.230, respectively. When a subset of the prior knowledge of the phantoms structure provided by the MRI was used in image reconstruction, the images that result indicate the presence of three material types, but quantitative accuracy is not optimal. When the full data set was utilized, and MR-derived priors guided the reconstruction, distinct boundaries separating each of the phantom layers were recovered. In this case, the rms error of the absorption and reduced scattering coefficient images decreased 43% to 0.0014, and 55% to 0.104, respectively. The ability to quantify deeply embedded regions was also greatly improved. The mean value of the absorption coefficient estimated in the region of the inclusion was accurate within 10% (0.018 mm^{-1} compared to the expected 0.02 mm^{-1}). Estimation of the reduced scattering coefficient improved to within 20% (0.9 mm^{-1} compared to the expected 0.75 mm^{-1}). This experiment indicated that resolution and accuracy were both improved with the added information about the layer, when implemented through a full regularization matrix. The algorithm responded to MRI-derived information about the structure of the imaged volume, and the spatial image patterns that it produced resembled that of the MRI. Note, however, that when a prior is specified, but no absorption or scattering contrast exists, the algorithm does not introduce artificial contrast within the image space matching the prior.

The second phantom study was completed to assess contrast-resolution. For the images shown in Fig. 4(b), when prior information is used in image reconstruction the rms error of the absorption and reduced scattering coefficient images decreased from 0.0019 to 0.0014 (26%) and from 0.1444 to 0.0613 (58%), respectively. The data plotted in Figs. 4(c) and 4(d) indicated that linearity exists between the estimated and the true contrast for the two reconstruction methods discussed here. A collection of intralipid solutions (primarily with different absorption coefficients) was imaged inside a homogeneous background of gelatin. MRI-guided reconstructions re-

covered more accurate property values over the entire range of contrast. Figure 4(b) showed that with MRI-guidance, image artifacts were suppressed (especially in μ_s' images). The error bars in Figs. 4(c) and 4(d) representing the NIR image pixel standard deviation indicated that the variation in the background and inclusion were reduced by using MRI priors.

An initial study of the breasts of normal volunteers has been conducted to assess the feasibility and comfort of the NIR array in the MR breast coil. Subject feedback indicated that the examination table is comfortable. As developed, the data acquisition system has proved feasible as well. We presented a single case study from the cohort of women imaged with our NIR-MRI system. MR images can distinguish adipose from glandular tissue with excellent contrast. This tissue discrimination was used as a prior and the two tissue types were treated separately in NIR image reconstruction. Figure 6 showed the detailed results from a typical volunteer exam. The same amplitude and phase data was processed three different ways, and Fig. 7 presented a quantitative summary of the results. Tissue parameters derived from spectral analysis ($[Hb_T]$, S_tO_2, water, A, and SP) were reported separately for adipose and glandular tissue. Error bars represented the standard deviation of property values within a particular tissue. For each chromophore, MR-guided NIR reconstruction decreased intratissue variation and increased intertissue contrast. For scattering parameters, MR guidance primarily reduced the size of the error bars. Adipose tissue in this subject appeared to be composed of 18-μM hemoglobin (approximately 0.75% blood volume, assuming an average 15.6 dL/L hematocrit), 80% oxygen saturation of the blood, and 15% water fraction. In the glandular tissue it appeared to be composed of 30-μM hemoglobin (approx. 1.25% blood volume), with 66% blood oxygen saturation, and 55% water fraction.

5 Conclusions

Phantom studies indicated that MRI can be used to improve the spatial resolution and quantitative accuracy of NIR parameter image reconstruction. In particular, by using an MR-guided iterative algorithm, layered structures can be recognized in diffuse media, and the properties of embedded objects can be studied with higher quantitative accuracy. Studies with a stand-alone NIR imaging system have shown that reconstructed tissue properties ($[Hb_T]$, A, and SP) correlate with tissue radiographic density.[8,18] Based on phantom studies presented here, which show that MRI-guided NIR characterization is more accurate, it is reasonable to conclude that the tissue characterization offered by the NIR-MRI system is preferred over stand-alone systems when available. The true values of these parameters in adipose and glandular tissue of individual subjects are not known, however, the trends observed in Fig. 6 and 7 are reasonable physiologically, when the MR information is encoded within the NIR reconstruction approach. Without the MRI, the potential to estimate NIR parameters for different tissues within the breast is not as accurate. The combined imaging approach may be particularly useful for breast lesion diagnosis or management, which will be the subject of future studies.

Acknowledgments

This work has been funded by NIH research grants RO1CA69544, PO1CA80139, and U54CA105480, and by the Department of Defense (DOD) breast cancer research program, DAMD17-03-1-0405.

References

1. D. T. Delpy and M. Cope, "Quantification in tissue near-infrared spectroscopy," *Philos. Trans. R. Soc. London, Ser. B* **352**, 649 (1997).
2. B. Chance, Q. Luo, S. Nioka, D. C. Alsop, and J. A. Detre, "Optical investigations of physiology: a study of intrinsic and extrinsic biomedical contrast," *Philos. Trans. R. Soc. London, Ser. B* **352**, 707 (1997).
3. S. Fantini, S. A. Walker, M. A. Franceschini, M. Kaschke, P. M. Schlag, and K. T. Moesta, "Assessment of the size, position, and optical properties of breast tumors *in vivo* by noninvasive optical methods," *Appl. Opt.* **37**, 1982–1989 (1998).
4. B. J. Tromberg, N. Shah, R. Lanning, A. Cerussi, J. Espinoza, T. Pham, L. Svaasand, and J. Butler, "Non-invasive *in vivo* characterization of breast tumors using photon migration spectroscopy," *Neoplasia* **2**, 26 (2000).
5. V. Ntziachristos and B. Chance, "Probing physiology and molecular function using optical imaging: applications to breast cancer," *Breast Cancer Res.* **3**, 41 (2001).
6. D. A. Boas, D. H. Brooks, E. L. Miller, C. A. DiMarzio, M. Kilmer, R. J. Gaudette, and Q. Zhang, "Imaging the body with diffuse optical tomography," *IEEE Signal Process. Mag.* **13**, 57–75 (2001).
7. B. W. Pogue, S. Geimer, T. O. McBride, S. Jiang, U. L. Osterberg, and K. D. Paulsen, "Three-dimensional simulation of near-infrared diffusion in tissue: boundary condition and geometry analysis for finite-element image reconstruction," *Appl. Opt.* **40**, 588 (2001).
8. S. Srinivasan, B. W. Pogue, S. Jiang, H. Dehghani, C. Kogel, S. Soho, J. J. Gibson, T. D. Tosteson, S. P. Poplack, and K. D. Paulsen, "Interpreting hemoglobin and water concentration, oxygen saturation, and scattering measured in vivo by near-infrared breast tomography," *Proc. Natl. Acad. Sci. U.S.A.* **100**, 12349 (2003).
9. M. F. Ernst and J. A. Roukema, "Diagnosis of non-palpable breast cancer: a review," *The Breast* **11**, 13 (2002).
10. T. Hata, H. Takahashi, K. Watanabe, M. Takahashi, K. Taguchi, T. Itoh, and S. Todo, "Magnetic resonance imaging for preoperative evaluation of breast cancer: a comparative study with mammography and ultrasonography," *J. Am. Coll. Surg.* **198**, 190 (2004).
11. P. A. Carney, C. J. Kasales, A. N. A. Tosteson, J. E. Weiss, M. E. Goodrich, S. P. Poplack, W. S. Wells, and L. Titus-Ernstoff, "Likelihood of additional work-up among women undergoing routine screening mammography: the impact of age, breast density, and hormone therapy use," *Prev. Med.* **39**, 48 (2004).
12. V. Chernomordik, A. H. Gandjbakhche, M. Lepore, R. Esposito, and I. Delfino, "Depth dependence of the analytic expression for the width of the point spread function (spatial resolution) in time-resolved transillumination," *J. Biomed. Opt.* **6**, 441 (2001).
13. H. Dehghani, B. W. Pogue, S. Jiang, B. A. Brooksby, and K. D. Paulsen, "Three-dimensional optical tomography: resolution in small-object imaging," *Appl. Opt.* **42**, 3117 (2003).
14. D. A. Boas, K. Chen, D. Grebert, and M. A. Francheschini, "Improving the diffuse optical imaging spatial resolution of the cerebral hemodynamic response to brain activation in humans," *Opt. Lett.* **29**, 1506 (2004).
15. P. S. Conti, D. L. Lilien, K. Hawley, J. Keppler, S. T. Grafton, and J. R. Bading, "PET and [18F]-FDG in oncology: a clinical update," *Nucl. Med. Biol.* **23**, 717 (1996).
16. M. Tatsumi, C. Cohade, Y. Nakamoto, and R. L. Wahl, "Fluorodeoxyglucose uptake in the aortic wall at PET/CT: possible finding for active atherosclerosis," *Radiology* **229**, 831 (2003).
17. A. L. Goertzen, A. K. Meadors, R. W. Silverman, and S. R. Cherry, "Simultaneous molecular and anatomical imaging of the mouse *in vivo*," *Phys. Med. Biol.* **47**, 4315 (2002).
18. B. W. Pogue, S. Jiang, H. Dehghani, C. Kogel, S. Soho, S. Srinivasan, X. Song, T. D. Tosteson, S. P. Poplack, and K. D. Paulsen, "Characterization of hemoglobin, water, and NIR scattering in breast tissue: analysis of intersubject variability and menstrual cycle changes," *J. Biomed. Opt.* **9**, 541 (2004).
19. B. W. Pogue and K. D. Paulsen, "High-resolution near-infrared to-

mographic imaging simulations of the rat cranium by use of *a priori* magnetic resonance imaging structural information," *Opt. Lett.* **23**, 1716 (1998).
20. R. L. Barbour, H. L. Graber, J. Chang, S. S. Barbour, P. C. Koo, and R. Aronson, "MRI-guided optical tomography: prospects and computation for a new imaging method," *IEEE Comput. Sci. Eng.* **2**, 63 (1995).
21. A. Li, E. L. Miller, M. E. Kilmer, T. J. Brukilaccio, T. Chaves, J. Stott, Q. Zhang, T. Wu, M. Choriton, R. H. Moore, D. B. Kopans, and D. A. Boas, "Tomographic optical breast imaging guided by three-dimensional mammography," *Appl. Opt.* **42**, 5181 (2003).
22. M. Schweiger and S. R. Arridge, "Optical tomographic reconstruction in a complex head model using *a priori* region boundary information," *Phys. Med. Biol.* **44**, 2703 (1999).
23. J. P. Kaipio, V. Kolehmainen, M. Vauhkonen, and E. Somersalo, "Construction of nonstandard smoothness priors," *Inverse Probl.* **15**, 713 (1999).
24. M. Vauhkonen, D. Vadasz, J. P. Kaipio, E. Somersalo, and P. A. Karjalainen, "Tikhonov regularization and prior information in electrical impedance tomography," *IEEE Trans. Med. Imaging* **17**, 285 (1998).
25. A. Borsic, W. R. B. Lionheart, and C. N. McLeod, "Generation of anisotropic-smoothness regularization filters for EIT," *IEEE Trans. Med. Imaging* **21**, 579 (2002).
26. X. Ouyang, W. H. Wong, V. E. Johnson, X. Hu, and C. Chen, "Incorporation of correlated structural images in PET image reconstruction," *IEEE Trans. Med. Imaging* **13**, 627 (1994).
27. V. Ntziachristos, A. G. Yodh, M. D. Schnall, and B. Chance, "MRI-guided diffuse optical spectroscopy of malignant and benign breast lesions," *Neoplasia* **4**, 347 (2002).
28. M. Glidewell and K. T. Ng, "Anatomically constrained electrical impedance tomography for anisotropic bodies via a twostep approach," *IEEE Trans. Med. Imaging* **14**, 498 (1995).
29. F. Dickin and M. Wang, "Electrical resistance tomography for process tomography," *Meas. Sci. Technol.* **7**, 247 (1996).
30. M. H. Loke, *Electrical Imaging Surveys for Environmental and Engineering Studies*, (1997). www.geo.mtu.edu/~ctyoung/LOKENOT.pdf
31. Q. Zhu, N. G. Chen, and S. H. Kurtzman, "Imaging tumor angiogenesis by use of combined near-infrared diffusive light and ultrasound," *Opt. Lett.* **28**, 337 (2003).
32. B. W. Pogue, H. Zhu, C. Nwaigwe, T. O. McBride, U. L. Osterberg, K. D. Paulsen, and J. F. Dunn, "Hemoglobin imaging with hybrid MR and diffuse optical tomography" in *Advanced Experiments in Medical Biology*, Ch. 21, pp. 215–224 (2003).
33. G. Gulsen, H. Yu, J. Wang, O. Nalcioglu, S. Merritt, F. Bevilacqua, A. J. Durkin, D. J. Cuccia, R. Lanning, and B. J. Tromberg, "Congruent MRI and near-infrared spectroscopy for functional and structural imaging of tumors," *Technol. Cancer Res. Treat.* **1**, 1 (2002).
34. B. A. Brooksby, S. Jiang, H. Dehghani, C. Kogel, M. Doyley, J. B. Weaver, S. P. Poplack, B. W. Pogue, and K. D. Paulsen, "Magnetic resonance-guided near-infrared tomography of the breast," *Rev. Sci. Instrum.* **75**, 5262–5270 (2004).
35. M. S. Patterson, B. C. Wilson, and D. R. Wyman, "The propagation of optical radiation in tissue II. Optical properties of tissues and resulting fluence distributions," *Lasers Med. Sci.* **6**, 379 (1991).
36. M. S. Patterson, B. C. Wilson, and D. R. Wyman, "The propagation of optical radiation in tissue I. Models of radiation transport and their application," *Lasers Med. Sci.* **6**, 155 (1991).
37. K. D. Paulsen and H. Jiang, "Spatially varying optical property reconstruction using a finite element diffusion equation approximation," *Med. Phys.* **22**, 691 (1995).
38. A. N. Tikhonov, "Regularization of mathematically incorrectly posed problems," *Sov. Math.* **4**, 1624 (1963).
39. H. Jiang, K. D. Paulsen, U. L. Osterberg, B. W. Pogue, and M. S. Patterson, "Optical image reconstruction using frequency-domain data: simulations and experiments," *J. Opt. Soc. Am. A* **13**, 253 (1996).
40. B. A. Brooksby, H. Dehghani, B. W. Pogue, and K. D. Paulsen, "Near-infrared tomography breast image reconstruction with a priori structural information from MRI: algorithm development for reconstructing heterogeneities," *IEEE J. Sel. Top. Quantum Electron.* **9**, 199 (2003).
41. T. O. McBride, B. W. Pogue, U. L. Osterberg, and K. D. Paulsen, *Oxygen Transport to Tissue XXIV*, p. 85 (2002).
42. G. Gindi, M. Lee, A. Rangarajan, and I. G. Zubal, "Bayesian reconstruction of functional images using anatomical information as priors," *IEEE Trans. Med. Imaging* **12**, 670 (1993).
43. B. A. Ardekani, M. Braun, B. F. Hutton, I. Kanno, and H. Iida, "Minimum cross-entropy reconstruction of PET images using prior anatomical information," *Phys. Med. Biol.* **41**, 2497 (1996).
44. J. E. Bowsher, V. E. Johnson, T. G. Turkington, R. J. Jaszczak, C. E. Floyd, and R. E. Coleman, "Bayesian reconstruction and use of anatomical a priori information for emission tomography," *IEEE Trans. Med. Imaging* **15**, 673 (1996).
45. C. Comtat, P. E. Kinahan, J. A. Fessler, T. Beyer, D. W. Townsend, M. Defrise, and C. Michel, "Clinically feasible reconstruction of 3D whole-body PET/CT data using blurred anatomical labels," *Phys. Med. Biol.* **37**, 1 (2002).
46. H. Xu, H. Dehghani, B. W. Pogue, R. Springett, K. D. Paulsen, and J. F. Dunn, "Near-infrared imaging in the small animal brain: optimization of fiber positions," *J. Biomed. Opt.* **8**, 102 (2003).
47. M. Torregrossa, C. V. Zint, and P. Poulet, "Effects of prior MRI information on image reconstruction in diffuse optical tomography," *Proc. SPIE* **5143**, 29–40 (2003).
48. X. Intes, C. Maloux, M. Guven, T. Yazici, and B. Chance, "Diffuse optical tomography with physiological and spatial *a priori* constraints," *Phys. Med. Biol.* **49**, N155 (2004).
49. K. D. Paulsen and H. Jiang, "Enhanced frequency-domain optical image reconstruction in tissues through total-variation minimization," *Appl. Opt.* **35**, 3447 (1996).
50. H. J. van Staveren, C. J. M. Moes, J. van Marle, S. A. Prahl, and M. J. C. van Gemert, "Light scattering in intralipid-10% in the wavelength range of 400–1100 nm," *Appl. Opt.* **30**, 4507 (1991).
51. A. E. Cerussi, A. J. Berger, F. Bevilacqua, N. Shah, D. Jakubowski, J. Butler, R. F. Holcombe, and B. J. Tromberg, "Sources of absorption and scattering contrast for near-infrared optical mammography," *Acad. Radiol.* **8**, 211 (2001).
52. S. Jiang, B. W. Pogue, T. O. McBride, M. M. Doyley, S. P. Poplack, and K. D. Paulsen, "Near-infrared breast tomography calibration with optoelastic tissue simulating phantoms," *J. Electron. Imaging* **12**, 613 (2003).